ApJ, in press, Jun 2012

The M31 Velocity Vector. I. Hubble Space Telescope Proper Motion Measurements

Sangmo Tony Sohn, Jay Anderson, and Roeland P. van der Marel

Space Telescope Science Institute, 3700 San Martin Drive, Baltimore, MD 21218

tsohn@stsci.edu

ABSTRACT

We present the first proper motion measurements for the galaxy M31. We obtained new V-band imaging data with the *Hubble Space Telescope* ACS/WFC and the WFC3/UVIS instruments of three fields: a spheroid field near the minor axis, an outer disk field along the major axis, and a field on the Giant Southern Stream. The data provide 5–7 year time baselines with respect to pre-existing deep first-epoch observations of the same fields. We measure the positions of thousands of M31 stars and hundreds of compact background galaxies in each field. High accuracy and robustness is achieved by building and fitting a unique template for each individual object. The average proper motion for each field is obtained from the average motion of the M31 stars between the epochs with respect to the background galaxies. For the three fields, the observed proper motions (μ_W, μ_N) are, in units of mas yr^{-1}, $(-0.0458, -0.0376) \pm (0.0165, 0.0154)$, $(-0.0533, -0.0104) \pm (0.0246, 0.0244)$, and $(-0.0179, -0.0357) \pm (0.0278, 0.0272)$, respectively. The ability to average over large numbers of objects and over the three fields yields a final displacement accuracy of a few thousandths of a pixel, corresponding to only 12 μas yr^{-1} . This is comparable to what has been achieved for other Local Group galaxies using VLBA observations of water masers. Potential systematic errors are controlled by an analysis strategy that corrects for detector charge transfer inefficiency, and spatially- and time-dependent geometric distortion and point-spread-function variations. The robustness of the proper-motion measurements and uncertainties are supported by the fact that data from different instruments, taken at different times and with different telescope orientations, as well as measurements of different fields, all yield statistically consistent results. Papers II and III of this series explore the implications of the new measurements for our understanding of the history, future, and mass of the Local Group.

Subject headings: proper motions — galaxies: individual (M31) — galaxies: kinematics and dynamics — Local Group

1. Introduction

At a distance of ~ 770 kpc (e.g., Freedman & Madore 1990), the Andromeda galaxy M31 is the nearest giant spiral to the Milky Way. Together, these two galaxies dominate the mass and dynamics of the Local Group. It is therefore of tremendous interest to determine the velocity vector of M31 with respect to the Milky Way. While the line-of-sight velocity of M31 is well-known from Doppler measurements, a determination of its proper motion (PM) has so far remained elusive.

The PM of M31 has been sought for almost a century (e.g., Barnard 1917), but *very high* astrometric accuracy is required to accomplish this. At the distance of M31, 100 km s^{-1} corresponds to 0.027 mas yr^{-1}. This is well beyond the accuracy limit of current ground-based optical observations even for long time baselines (e.g., > 40 year; e.g., Vieira et al. 2010). The two most accurate (~ 0.01 mas yr^{-1}) PM measurements in the Local Group come from studies of water masers in M33 (Brunthaler et al. 2005) and IC 10 (Brunthaler et al. 2007). However, water masers in M31 have only recently been discovered (Darling 2011), and it will take time until a sufficient baseline has been established to enable PM measurements.

Theoretical modeling of the local Universe has suggested that the Galactocentric rest-frame velocity of M31 must have a tangential component $V_{\rm tan} \leq 200$ km s^{-1}. However, within this limit many different orbits are still possible (Peebles et al. 2001). van der Marel & Guhathakurta (2008) recently presented an estimate of M31's transverse velocity based on indirect arguments, using the known kinematics of satellite galaxies of M31 and the Local Group. Their estimate implies that $V_{\rm tan} \leq 56$ km s^{-1}, at 68.3% confidence. In other words, M31 may be moving directly (radially) towards the Milky Way. This might have drastic implications for the future of the Milky Way, and even for the Sun itself (Cox & Loeb 2008). However, all theoretical and indirect estimates of $V_{\rm tan}$ make assumptions about the structure and equilibrium of the Local Group that may not hold true in our hierarchically-evolving universe. Therefore, only a direct PM measurement will yield a robust determination of the M31 velocity vector.

The *Hubble Space Telescope* (*HST*) is an observing platform in space with unparalleled astrometric capabilities. Whereas the *absolute* astrometric accuracy of *HST* is limited by the accuracy of the Guide Star Catalog (~ 0.2 arcsec for GSC2.3; Lasker et al. 2008), the current

onboard imagers of *HST* (e.g., ACS and WFC3) are capable of measuring *relative* positions of multiple sources in a field to better than 0.5 mas. Therefore, it is possible to measure very accurate absolute PMs of stars by measuring their displacement over time relative to stationary background reference source(s) in the same field.

Quasi-stellar objects (QSOs) have conventionally served as reference sources in *HST* PM studies, due to their star-like appearance and luminous nature. Such a strategy has been used in several studies for measuring absolute PMs of Milky Way satellite galaxies (e.g., Piatek et al. 2002, 2003, 2005, 2006, 2007; Kallivayalil et al. 2006a,b; Piatek et al. 2008). However, the accuracies thus achieved are not sufficient at the distance of M31. This is due in part to drawbacks of using QSOs. Not only must they be spectroscopically identified in advance, but their distribution on the sky is sparse. For the small field of view of *HST* imagers, these limits require the observer to find a QSO behind the field of interest. If one exists, one must deliberately image the field containing the QSO at two or more different epochs to measure the displacement of the stars relative to the QSO. Even then, the PM uncertainty is limited by the positional accuracy of a single QSO.

Instead of using QSOs, one can use background galaxies as reference objects in *HST* studies of absolute PMs. At the spatial resolutions of interest here, these sources are also stationary due to their large distances. One great advantage of background galaxies is their ubiquity: background galaxies are found in nearly every deep astronomical image. Moreover, using many background galaxies can provide higher accuracy than using a single QSO. While the individual positional accuracy is somewhat poorer for galaxies, their much larger number provides an important $\sqrt{N}$ advantage in averaging. For example, Milone et al. (2006) and Kalirai et al. (2007) used background galaxies to derive an accurate PM of the Galactic globular cluster NGC 6397, at the distance of ~ 3 kpc from the Sun. Similarly, Brown et al. (2010) used background galaxies to determine the absolute PM of a hypervelocity star in the Milky Way halo.

Unlike the situation with QSOs, galaxy positions are difficult to measure. One can adopt a simple centroiding algorithm, but such algorithms have limited accuracy in the undersampled images of *HST*'s wide-field detectors (Anderson & King 2000). Furthermore, the resolved galaxies and the unresolved stars would be expected to have different centroid biases, leading to spurious apparent PMs. As a better alternative, Mahmud & Anderson (2008) developed a template-fitting method to measure accurate positions of resolved background galaxies. In this method, a tailor-made template is constructed for each individual object, and the same template is used to measure a consistent position for that object in each exposure. This is conceptually similar to the effective point spread function (ePSF) approach widely used for stars (Anderson & King 2000). Even for bright background galaxies,

the template-fitting method is able to measure positions at least twice as well as with simple centroids (Mahmud & Anderson 2008).

In this paper we present the first proper motion measurements for the galaxy M31, based on new *HST* ACS/WFC and the WFC3/UVIS imaging of three fields with deep pre-existing data. We use the template-fitting method of Mahmud & Anderson (2008) as our basis, but make several innovations in the analysis to minimize systematic errors and ensure robustness of the results. The final accuracy of only 12 μas yr^{-1} is significantly better than what has been achieved by *HST* for other nearby galaxies, and is comparable to what has been achieved for other Local Group galaxies using VLBA observations of water masers.

This paper is organized as follows. Section 2 describes the observations. Section 3 describes the analysis steps that lead to the PM measurements. Section 4 presents and discusses the PM results thus obtained for the three target fields. Concluding remarks are presented in Section 5.

This is the first paper in a series of three. In Paper II (van der Marel et al. 2012) we derive the velocity vector of the M31 center of mass by correcting the PM results presented here for the internal motions of stars within M31 and for the reflex solar motion. We then combine the result with other estimates to determine the Galactocentric velocity and orbit of M31, and use this to estimate the mass of the Local Group. In Paper III (van der Marel et al. 2012b, in preparation) we use the results to study the future dynamical evolution of the Local Group, and the expected merging of the Milky Way-M31-M33 System.

2. Data

2.1. First-Epoch Data

The data set we used for measuring the PM of M31 consists of *HST* images of three fields obtained in two separate epochs. The fields are the **SPHEROID**, **OUTERDISK**, and **TIDALSTREAM** fields of Brown et al. (2006) obtained under the science programs GO-9453 and GO-10265 (PI: T. Brown). Figure 1 shows the location of the three M31 target fields. The observation details for the first epoch data are given in Brown et al. (2006); field coordinates and total exposure times are listed in their Table 1. In brief, the target fields were observed between December 2002 and January 2005 in two filters (F606W and F814W) with HST ACS/WFC to create color-magnitude diagrams (CMDs) that reach well below the M31 main sequence turn-off. For each field, all exposures were obtained within 40 days so they can be safely treated as a single epoch of data. Total per-field per-filter exposure times ranged from 53-161 ksec. Individual images had exposure times ranging from 1,100

to 1,300 sec, and were dithered such that no two exposures placed a star on the same pixel. In addition to the whole-pixel offsets, the dithering strategy also included sub-pixel shifts so that every object was observed at a range of locations relative to the pixel boundaries; such "pixel phase" coverage is critical for our program. The very deep first-epoch F606W data were used by us for constructing super-sampled stacked images, identifying stars and galaxies, building templates for the template-fitting method, and providing reference positions of stars and galaxies, as described in Section 3 below.

2.2. Second-Epoch Data

Our second-epoch data were observed between January 2010 and August 2010 using ACS/WFC and WFC3/UVIS in F606W (HST program GO-11684, PI: van der Marel). We designed our observations to minimize random and systematic errors with the following strategies in mind. Pre-analysis of the first-epoch data revealed that the F606W filter provides slightly better astrometric handle on the background galaxies than the F814W filter, so we chose to obtain second-epoch images only with F606W. Furthermore, we decided to observe the three target fields with two different instruments instead of just one. This yields comparable random error, but allows additional consistency checks on our PM results. Since the purpose of the second-epoch observations was astrometry, and not deep photometry, the total second-epoch exposure time was much less than in the first-epoch. We observed each target field for two orbits (four half-orbit exposures) with WFC3/UVIS and one orbit (two half-orbit exposures) with ACS/WFC. Individual images had exposure times ranging from ∼1,300 to 1,500 sec, slightly longer than in the first epoch, and were dithered in similar fashion. The baselines between the two epochs are in the range of 5–7.5 years.

For the ACS observations, we used the same orientations and coordinates as used by the first-epoch observations to maximize the overlapping area and so that any errors in the static distortion solution would naturally cancel out. Due to different sets of guide stars being used between the first- and second-epoch observations, the second-epoch ACS images were slightly offset and rotated with respect to the first-epoch images. However, the offsets are all within a negligible fraction of the ACS/WFC field of view (FOV), and the orientations are within $0.^{\circ}1$ of each other.

For the WFC3 observations, we pointed the telescope so that the resulting images roughly share the same centers with the first epoch, but the WFC3 images were rotated by roughly 45° with respect to the ACS images. This was to place the parallel ACS/WFC fields overlapping with the first epoch parallel WFPC2 images, but the parallel fields will not be discussed in this paper as they are not useful for astrometry at the accuracy that

we need. Because the FOV of WFC3/UVIS is 64% of that of the ACS/WFC, the observed WFC3 images are fully contained within the ACS images despite the $\sim 45^{\circ}$ difference in their orientations. The details of our second-epoch data are summarized in Table 1.

3. Analysis

3.1. Overview

Measurement of proper motions involves measuring the displacement between the position of an object at one time and its position at another. If this displacement can be measured with respect to objects for which we know the absolute motion, then we can obtain absolute PMs. In our case, we will measure the displacement of M31 stars with respect to the background galaxies in the field to obtain an absolute PM. Our strategy is to first align the stars in the first- and second-epoch images, restricting the alignment to those stars confirmed to belong to M31. Then we measure the average displacement of the background galaxies with respect to this moving frame of reference. The negative of this relative displacement yields the mean absolute PM of the M31 stars. This measurement of the mean does not require knowledge of the exact PM *distribution* of the M31 stars. This distribution can be complex, because different structural components of M31 contribute to each field. However, to transform the mean PM of the M31 stars in a field to an estimate of the M31 center of mass, one does need to construct a model for the internal kinematics of M31, which is addressed in Paper II of this series.

The overall PM derivation process is summarized below.

1. We first create a high-resolution stacked image using the deep and well-dithered first-epoch images for each target field using the distortion-corrected first exposure as the reference frame.

2. Stars and galaxies are then identified from the stacked image for each field, and photometric measures and the CMD are used to specifically identify M31 reference stars.

3. We construct a template for each star and galaxy from the high-resolution image.

4. We then use the template to measure in a consistent fashion a position for each star/galaxy in each individual exposure of each epoch.

5. We redefine the first-epoch reference frame using the template-based positions of the stars, and determine the average first-epoch position of each galaxy in this frame.

6. We determine the template-measured positions of the stars in each of the six second-epoch exposures for each field and use them to transform the template-measured positions of the galaxies into the first-epoch frame.

7. We then take the difference between the second- and first-epoch positions of the galaxies to obtain the relative displacement of the galaxies with respect to the M31 stars.

8. Finally, we multiply the relative displacements of the galaxies by -1 to obtain the mean absolute displacement of the M31 stars, since in reality the galaxies are stationary and the stars are moving. Division by the time baseline turns the displacements into PMs.

The following sections provide the details of each step.

3.2. Initial Processing of Individual Exposures

We downloaded all the required data in the form of `_flt.fits` images from the STScI *HST* archive. These images are already bias-subtracted, dark-subtracted, and flat-fielded by the STScI data-reduction pipelines using the best available calibration data at the time of data inquiry. Each multi-extension `_flt.fits` file was converted to a single 4,096×4,096 image where the top chip scene is directly abutted to the bottom chip scene. This single-format image allows a more efficient way of handling the data, and all computer software we used throughout our analysis were specifically programmed to deal with this image format.

The *HST* detectors suffer from significant degradation in charge-transfer efficiency (CTE) as time progresses. This impacts the astrometry of objects by effectively shifting the centroid position of the flux distribution. This can be a particularly serious problem for our second-epoch ACS/WFC data, taken almost 9 years after the installation of ACS. A pixel-based CTE correction routine has recently been developed by Anderson & Bedin (2010) for the ACS/WFC, and Brown et al. (2010) demonstrated that this correction works very well for astrometric purposes. All first-epoch ACS/WFC images were processed through this routine. For the second-epoch ACS/WFC images, we used a modified version of the CTE correction code that also included a correction for X-CTE, in addition to the publicly available correction for Y-CTE. We found that the X-CTE correction made very little difference to the positions measured in the images, compared to the other uncertainties in the results.

A CTE correction routine was not available for the WFC3/UVIS at the time of writing this paper, so no correction was made to the WFC3 images. However, since at the time of the observations, UVIS had spent only $\sim 10\%$ as much time as ACS in the space environment, the CTE degradation of our UVIS images is expected to be quite small. Although UVIS appears

to be losing charge-transfer efficiency faster than ACS did, the studies that show this have focused on low-background images (e.g., Baggett et al. 2011). As our backgrounds are quite high, we expect CTE losses to be very low for our images. Hence, the CTE degradation should only have a minimal effect on our WFC3 PM measurements. A direct post-facto consistency check of this is provided by comparison our ACS/WFC and WFC3/UVIS PMs derived for the same fields (see Section 4.2 below).

As the final step of the initial processing of individual images, we measured each star using the `img2xym_WFC_9x10` program (Anderson & King 2006) on the ACS/WFC images, and using a similar program on the WFC3/UVIS images. Both programs utilize library PSFs to determine a position and a flux for each star. We will use these PSF-based star positions to provide our initial handle on the coordinate transformations from one image to another.

3.3. Distortion Corrections

The positions of objects on the *HST* detectors must be corrected for geometric distortions before they can be used for any astrometric measurement. For the ACS/WFC detector, the distortion-correction solutions by Anderson (2005) have been used in several astrometric studies. These solutions are known to be better than 0.01 pixel or ∼0.5 mas, and were shown to be stable between 2002 and 2007 (Anderson 2007; van der Marel et al. 2007). These available solutions were directly applied to the positions measured in our first-epoch ACS/WFC images.

While reducing data for another program (GO-11677, PI: H. Richer), one of us (J.A.) found that the ACS distortion solution appears to have changed by ~ 0.005 pixel relative to the solution before the *HST Service Mission 4* (SM4). This may be related to a similar variation of the PSF (Anderson et al., in prep.). It is unclear what caused these variations, but they appear to be stable over time. We used the GO-11677 data set to develop a correction to the pre-SM4 ACS/WFC distortion solution and applied it to the second-epoch data. For the WFC3/UVIS data, we used the distortion corrections provided by Bellini et al. (2011). These corrections are better than 0.008 pixel or ∼0.3 mas and appear to be stable over the UVIS lifetime so far.

The accuracies of the distortion corrections are comparable to our final measured motions (as will be shown later). However, geometric distortion affects both star and galaxy positions similarly, and hence drops out in a differential measurement to lowest order. This is true in particular if each galaxy position is measured with respect to that of nearby stars

that fall on the same area of the detector. This is what we do in Section 3.8 below, to ensure that higher order geometric distortion correction residuals do not affect our final results.

3.4. Stacked Images

The deep and well-dithered first-epoch ACS/WFC data are well-suited for constructing high-resolution stacked images. To do this, we first apply the distortion corrections (see Section 3.3) to the positions of stars measured in Section 3.2. We then adopt the first exposure of each field as the frame of reference, cross-identify stars in this exposure and stars in the other exposures, and use their distortion-corrected positions to construct a six-parameter least-squares linear transformation between the two frames. The six parameters involve x-y translation, scale, rotation, and two components of skew. The need for these linear transformations is discussed in Section 3.6.4 of Anderson & van der Marel (2010). We use these transformations to convert the star positions measured in the various images into the reference frame, giving us many estimates of the position of each star in the reference frame. We average these positions to refine the reference-frame positions for all the stars, and use these new average positions to improve the transformations (which had initially been based on the positions as measured in the first frame itself). This procedure is iterated 2–3 times to improve the positions of both the stars and the transformations.

We use the star-based transformations to construct the stacked images. In order to get better sampling, we super-sample the stacked image by a factor of 2 relative to the native ACS/WFC pixel scale. The image-stacking process we used is similar to the commonly used `Drizzle` algorithm (Fruchter & Hook 2002) with a point kernel, except that we included an iterative procedure to regularize the sampling in a manner similar to `iDrizzle` (Fruchter 2011). The procedure involves no deconvolution, and as such the resulting image at every point simply represents the flux that an actual `_flt` image pixel would receive if it were centered at that location in the frame. It is this property that allows us to construct empirical templates (see Section 3.6.1) for our stars and galaxies. Figure 2 shows a $25'' \times 25''$ portion of the $2\times$ super-sampled stacked image for the *SPHEROID* field with M31 stars and background galaxies identified, as described in the following sections.

3.5. Identifying Stars and Galaxies

All of our target fields are dominated by M31 stars, but there are also other sources, such as foreground stars and background galaxies. Since our strategy for deriving the PM of M31

is to measure the displacement of the background galaxies relative to the co-moving frame of reference defined by the M31 stars, it is important to accurately identify both background galaxies and M31 stars before we proceed any further.

3.5.1. Identifying M31 Reference Stars

The selection of M31 stars was carried out following the procedure below. For each target field, we use the star list compiled in Section 3.4. Our initial star lists include only sources that are found independently in a large number of first-epoch F606W exposures (typically, $> 35\%$); as such, the list is almost entirely free of cosmic rays and image defects. There are, however, a large number of resolved sources, which could be either blended stars or extended background galaxies. To identify them, we made use of the mean quality-of-PSF-fit parameter (`QFIT`) reported by the `img2xym_WFC_9x10` program (see Figure 3a). Selecting the objects with low values of `QFIT` allows us to filter out extended objects as well as stars that are too close to other stars to provide accurate position measurements. To ensure that all of the stars in the list are M31 members, we reduced the F814W images and constructed a CMD (see Figure 3b). From this, we selected stars that lie roughly on the M31 sequences. Although small in number, field stars in the Milky Way halo may be included in our selection, but we believe that most of them will be filtered out in our next step of selection. Finally, reference stars were selected based on their lack of motion with respect to the other M31 stars. This was done by aligning the second-epoch star positions with the first-epoch positions and iteratively rejecting the objects that have moved between the epochs (see Figure 3c). For any given ACS/WFC target field, the M31 stars should all be moving towards the same direction in space. Differential motions due to the internal kinematics of M31 within a single ACS/WFC field should be negligible compared to the observational uncertainties (see Paper II for details). We note that, in principle, better detection and photometry of fainter stars can be achieved by measuring stars directly from the stacked images as has been demonstrated by Brown et al. (2006). However, as our main goal is doing astrometry, we are only interested in stars for which positions can be reliably measured in *individual exposures*. Our final lists of M31 reference stars include $\sim 10,000$ stars for the **SPHEROID** and **OUTERDISK** fields, and $\sim 5,000$ stars for the **TIDALSTREAM** field.

3.5.2. Identifying Background Galaxies

A quick visual inspection of the super-sampled stacked images of our target fields reveals that there are hundreds of background galaxies. We have already identified sources using the `img2xym_WFC_9x10` program, but because that program is specifically designed to measure stars, it neglects many of the extended sources. For this reason, `SExtractor` (Bertin & Arnouts 1996) was separately run on the stacked images to detect and measure extended sources. We generated a candidate list of galaxies by selecting sources from the `SExtractor` output mainly based on their `MAG_AUTO`, `CLASS_STAR`, and `FLUX_MAX` parameters. For each field, this candidate list included more than 1,000 sources, but we found that many of the candidates are in fact multiple stars clustered together. We carefully identified sources in the candidate list one by one, basing our judgment on their 2-d contours and 3-d surface profiles. Whenever the identification was unclear, we excluded the source from our selection to stay on the conservative side. We note that we desire the background galaxy list to be as free of contamination by stars as possible because the PM measurements are sensitive to the reference sources we choose to use. Finally, we considered only objects for which the template-fitting method, described in the next section, yields position uncertainties of less than 0.25 pixel in both X and Y. The final lists contain 368, 339, and 374 galaxies for the **SPHEROID**, **OUTERDISK**, and **TIDALSTREAM** fields, respectively.

3.6. Measuring Positions of Objects with Templates

Our goal is to measure accurate PMs. The most crucial part of our analysis is therefore to measure the positions of objects in the individual images as accurately as possible. Simple methods such as fitting the objects with a two-dimensional Gaussian function or finding the flux centroid are accurate only if the objects have well-sampled peaks. This is not the case for most of the background galaxies in our target fields. To measure the positions of objects, we therefore adopt the template-fitting method developed by Mahmud & Anderson (2008).

3.6.1. The Template-Fitting Method

The details and general diagnostics of the template-fitting method are documented in Mahmud & Anderson (2008). Here we summarize only the basic concepts behind the method. The distortion corrections in Section 3.3 and the linear transformations derived in Section 3.4 allow us to associate a position $(x_r, y_r)_j$ in a given individual image j with a position (x_m, y_m) in the stacked image, and *vice versa*. We are thus able to build a model

of what the galaxy or star should look like in an individual image by proper sampling of the stacked image.

The goal is to measure in consistent fashion a position for each object (star or galaxy) in each individual exposure. To do this, we construct a template model for each object, and use it to measure that object in every exposure. The location within the template that we will define to be its center is arbitrary, since in the end we care only about differences in position. So we define the center of the brightest pixel in the stacked image to be the object center (or "handle" in the parlance of Mahmud & Anderson). With the center so defined, we interpolate the stacked image at a super-sampled array of points, with the center at (0,0) but with a pixel orientation and spacing that corresponds to the transformed exposure's `_flt` coordinate system. The result is a template that can be interpolated at an array of locations to tell us how much flux we would expect in an array of `_flt` pixels for a presumed object center. The template is custom-made for each individual exposure, based on the mapping of that exposure's pixel coordinate system into the master frame. The template centers are all the same.

For each object in each exposure, we use the previously established transformations to identify the location of the object in the exposure to within one pixel. We then evaluate an array of trial locations for the center, covering an area of 1×1 pixels with a spacing of 0.01 pixel. At each trial location, interpolation of the template with a bicubic interpolation algorithm tells us how much flux we should expect to measure in each pixel of the exposure. We compare this model to the actual observed pixel values to obtain a quality-of-fit quantity,

$$qfit_{ij} = \frac{\Sigma_{\rm pixels} |OBS - MODEL_{ij}|}{\Sigma_{\rm pixels} OBS}, \tag{1}$$

for each trial offset (i, j). The position of the galaxy or star then corresponds to the location of the template center that gives the minimum $qfit_{ij}$.

In Section 3.2 we used empirical "library" PSF fits to the stars to define the transformations for construction of the stacked images. However, for the final PM measurements we use the template procedure for both galaxies and stars. This minimizes any potential for systematic errors due to differences in measurement techniques between different types of objects. The sums in equation (1) were chosen to extend over the 5×5 pixel raster centered on the object's brightest pixel in the individual exposure. The size of this region was deliberately chosen to be small, since most of the positional information for the stars and compact galaxies of interest here is contained in the central core pixels.

3.6.2. First-Epoch ACS Data

We applied the template-fitting method to all stars and galaxies in the first-epoch ACS/WFC data, to determine their positions in each exposure. To illustrate the quality of the template-fitting method, we show in Figure 4 the best fit $qfit$ (as defined in Section 3.6.1) versus instrumental magnitude for the background galaxies in one of the first-epoch images. The top row of Figure 5 shows the data, template fits, and residuals for three galaxies of different brightness, and for one star.

3.6.3. Second-Epoch ACS Data

The stacked images constructed in Section 3.4 represent the astronomical scene convolved with the average effective PSF *appropriate for the first-epoch data*. The effective PSF represents the convolution of the instrumental PSF with the sensitivity profile of a pixel. The astronomical scene for any given object should not change between our epochs of data, but the effective PSF might change. This is certainly the case for the second-epoch WFC3/UVIS data, discussed below, since both the instrumental PSF and the pixelization are different than for the first-epoch ACS/WFC data. However, we also found that the effective PSF for the second-epoch ACS/WFC data was not the same as for first-epoch ACS/WFC data. Even though the pixelization remained the same, we found that a subtle change occurred in the ACS PSF since SM4 (see Section 3.3).

It is important that any change in the effective PSF be explicitly accounted for in the analysis. PSF changes can introduce centroid shifts, and these shifts can be different for point sources and for extended sources. Our technique for measuring the M31 PM relies on positional differences between stars and background galaxies. PSF changes can therefore produce spurious PM results.

In order to deal with the differences in the effective PSF between epochs, we model each object in a given second-epoch image as follows. First, we select bright and isolated stars from the M31 reference star list compiled in Section 3.5.1 , and use them to derive a 7×7-pixel kernel that accounts for differences in effective PSF between the stacked image and the individual exposure. Next, we interpolate the first-epoch template onto the `_flt` pixel grid of the second epoch image, as we did in Section 3.6.2. We then convolve the template with the kernel derived in the earlier stage, and finally evaluate the goodness-of-fit quantity $qfit$ to find the object position that provides the minimum $qfit$. The middle row of Figure 5 shows the data, template fits, and residuals for three galaxies of different brightness, and for one star, obtained with this procedure for one of the second-epoch ACS/WFC images

(jb4404vuq).

The complexity in this procedure lies in the determination of the kernel. Each kernel has 49 free parameters. However, it is constrained by 5×5-pixel patches centered around *all* the objects in each image. This is an over-determined problem that can be solved to find the best-fitting kernel. We cast the problem into the form of a least-squares matrix equation, and solved for the kernel using the observed pixel values for several thousand bright and isolated stars distributed throughout the target fields. The solution was obtained through *singular value decomposition* (Press et al. 1992). To fit the kernels, we first determined the stellar positions of the bright and isolated stars without any kernel. Then we kept those positions fixed, and optimized the kernels.

We ended up using a single kernel for each second-epoch image. We experimented with using different kernels for different parts of each image (to deal with potential field-dependent PSF variations), but found that this did not change the main results. In deriving the kernel, we recognized that there is a degeneracy between shifting the kernel and shifting the astronomical scene. We removed this degeneracy by constructing the pixel residuals that went into the kernel with respect to the library-PSF-measured position (see Section 3.2) for each star. This ensured that the kernel would reproduce on average the PSF-based positions for the stars, and that it would properly account for changes in source shape due to known PSF variations between epochs. Either way, the degeneracy does not affect absolute PMs that are based on relative differences in position between stars and background galaxies.

The top panels of Figure 6 show the average of the derived normalized kernels for the second-epoch ACS/WFC images. Slight asymmetries are evident, primarily in the X direction. Without our kernel-based corrections, such asymmetric PSF differences would bias astrometry.

3.6.4. Second-Epoch WFC3 Data

Our second epoch WFC3/UVIS images are rotated by $\sim$ 45 deg with respect to the ACS images. Because we have many bright M31 stars in the field, we are able to derive six-parameter linear transformations that relate the undistorted WFC3 positions to the stacked image without difficulty.

To determine the positions of all objects in the field we used the same kernel-based template-matching approach as for the second-epoch ACS data. In this case, the kernel accounts not only for PSF variations, but also for variations in the PSF size and orientation between epochs. The bottom row of Figure 5 shows the data, template fits, and residuals

for three galaxies of different brightness, and for one star, obtained with this procedure for one of the second epoch WFC3/UVIS images (`ib4401s1q`).

The kernel size for the WFC3/UVIS data was chosen to be the same as for the ACS data, and we used over 1,000 stars to derive the kernels. The bottom panels of Figure 6 show the average of the derived normalized kernels for the second-epoch WFC3/UVIS images. There are slight asymmetries in both coordinate directions. This differs from the situation for the second-epoch ACS/WFC data, because the WFC3/UVIS detector is rotated by $\sim 45^{\circ}$ in the HST focal plane with respect to the ACS/WFC detector. Also, the symmetric part of the kernels differs between the second-epoch ACS/WFC images and the second-epoch WFC3/UVIS images. This is because of the difference in PSF shapes between the different detectors. Our kernel-based approach minimizes potential systematics arising from measuring positions of stars and galaxies in images with different PSF characteristics.

Our PM measurement technique for each field compares the high-resolution stacked image from the first-epoch to the individual exposures from the second epoch. The derived kernels account for variations in the average PSF between the epochs, as well as exposure-to-exposure PSF variations within the second epoch. We do not compare second-epoch exposures to individual first-epoch exposures, but only to the high-resolution stacked image. The stacked image is constructed from the first-epoch images, so on average, the PSF does not change between the stacked image and the individual first-epoch images. Therefore, any exposure-to-exposure PSF variations that may exist within the first epoch do not affect the derived PMs. For this reason, there was no need to study or correct explicitly PSF variations within the first epoch data set.

3.7. Reference-Frame Positions and Positional Uncertainties

The processes outlined above lead to accurate positions of stars and galaxies in each individual exposure. We align the star positions between exposures using the same iterative approach described in Section 3.4, but this time using the newly derived positions based on the template-fitting method instead of the initial library-PSF-based positions. For each exposure for a given field, this procedure yields a six-parameter linear-transformation with respect to the first exposure in the first epoch for that field. For all objects (stars and background galaxies) in all exposures, we apply the known geometric distortion solutions and these linear-transformations, to obtain the position in the distortion-corrected frame of the first exposure (i.e., `j8f801abq`, `j92c01b4q`, and `j92c28ccq` for **SPHEROID**, **OUTERDISK**, and **TIDALSTREAM**, respectively). These distortion-corrected frames serve as our reference frames.

In the first-epoch data we have many exposures. This yields multiple determinations for the position of each star or galaxy in the reference frame. The RMS scatter among these determinations provides a measure of the random positional uncertainty in a single measurement for each object. Figure 7 shows the one-dimensional errors in positions for M31 stars (upper panels) and background galaxies (lower panels) as a function of instrumental magnitude (defined as $m_{\rm instr} = -2.5\log[\text{electrons}]$) in the three separate target fields. Brighter objects have a higher signal-to-noise ratio than fainter objects, and therefore have more accurately determined positions. Stars are more compact than background galaxies, and therefore also have more accurately determined positions. At fixed magnitude, the scatter in positional accuracy is larger for the galaxies than for the stars. This is because galaxies have a large variation in sizes and shapes, with the morphology also depending on wavelength. The dependence of astrometric accuracy on size and shape was discussed in Sohn, Anderson, & van der Marel (2010), and the dependence on wavelength was discussed in Mahmud & Anderson (2008). At the bright end in Figure 7, the per-exposure accuracies level off at 0.01–0.02 WFC pixels for both stars and galaxies. When many measurements are averaged, the positional errors decrease as $1/\sqrt{N}$.

3.8. Proper Motions of Individual Objects

Using the above procedure,we determine for each object its average first-epoch position in the reference frame. In a similar way, we measure template-based positions for each second-epoch exposure, correct these positions for distortion, and transform them into the reference frame using the template-measured star positions. We then compare these positions with the first-epoch averages to estimate the PM displacement for that object. Division by the time baseline of the observations then yields an estimate of the actual PM.

By construction, our method aligns the star fields between epochs. M31 stars will therefore have zero PM on average. Figures 8 and 9 show the residual motion of each star in X and Y (PM_X and PM_Y) as a function of chip coordinates for one of the second-epoch ACS/WFC images, and for one of the second-epoch WFC3/UVIS images. These plots show that the "average star" (given our selection criteria and brightness limits) is measured with a precision of ~ 0.05 pixel (but as shown in Figure 7, this is a strong function of brightness). When averaging over an ensemble of N stars in M exposures, the accuracy of the average PM is in principle smaller by a factor $\sqrt{NM}$. The stellar PMs show that there remain some small systematic trends with position on the detector, at levels $\lesssim 0.02$ pixel. These trends may be related to small changes in the distortion solution between the first and second epochs, or other low-level systematic effects that are not accounted for in our analysis. Such systematic

trends might affect PM results. It is therefore important that we correct for them. We note that we found similar residual trends in all three target fields. This indicates that whatever is causing the low-level systematic trends is related to the detector characteristics rather than the internal kinematics of M31.

The background galaxies were not used to define any transformations between the first-epoch and second-epoch data. Any motion between the galaxies and stars should therefore show up as a displacement between the first- and second-epoch galaxy positions in the reference frame. We measure these displacements in a two step process to remove any systematic PM trends related to the position on the detector, such as those visible in Figures 8 and 9.

First, we calculate the difference between the first- and second-epoch positions for each background galaxy in the reference frame. Then, for each galaxy, we compute the average displacement of stars in the vicinity of the galaxy. We subtract this displacement from the galaxy displacement. This "local correction" ensures that the displacement of each background galaxy is measured only with respect to the M31 stars that fall on the same part of the detector. This removes any remaining systematic PM residual associated with detector position. Each local correction is constructed using stars of similar brightness (± 1 mag in the inner 5×5 pixels area) and within a 200 pixel region centered on the given background galaxy. The matching of the stars and background galaxies in brightness was motivated by the fact that some known detector effects (such as CTE), depend not only on detector position, but also on the source brightness.

In the top panels of Figures 10 and 11, we show the X and Y proper motions (PM_X and PM_Y) of each galaxy as a function of chip locations (X and Y), for the same second-epoch exposures as in Figures 8 and 9. There are many more stars than background galaxies in each frame, and the positions of the stars are generally more accurately determined than those of the galaxies (see Figure 7). The final PM error for each second-epoch exposure is therefore dominated entirely by the astrometric accuracy for the background galaxies.

4. M31 Proper Motion

4.1. Final Results

To determine an average PM of the M31 stars in each field, we start with the measured PM displacements of the background galaxies in the reference frame (including local corrections as described above). For each of the 18 different second-epoch images, we calculate the weighted average using the positional errors determined from the RMS among the first-

epoch measurements. Outliers were rejected in this process with an iterative 3-σ rejection scheme applied to the 2-d PM distribution. The uncertainty of the average was computed using the bootstrap method (Efron & Tibshirani 1993) with 10,000 bootstrap samples for each case. This provides a rigorous error estimate, which is ultimately based on the actual scatter between results inferred from different background galaxies. This naturally includes any random errors due to photon-counting statistics, as well as any potentially remaining systematic errors that lead to increased scatter (but any systematic errors that affect all sources equally would not be quantified by this).

We then transformed the results to average PMs (and their associate errors) of M31 stars in the directions north and west, in units of mas yr^{-1}. To do this, we used the orientation of the reference image (see Section 3.6.2) with respect to the sky (using the FITS header keyword ORIENTAT), the time baseline, and the fact we are measuring the relative displacement of the background galaxies with respect to the M31 stars in our target fields. In Table 2, we tabulate the PM[1] (μ_W, μ_N) inferred from each second-epoch image and the corresponding error, along with the number of background galaxies used for the PM derivation. Figure 12 shows for each of the three target fields the PM estimates inferred from the six independent second-epoch exposures (2 ACS/WFC + 4 WFC/UVIS).

The final estimate of the average PM of the M31 stars in each field is calculated by taking the error-weighted mean of the six independent measurements listed in Table 2. The results are shown in red in Figure 12, and they are tabulated in Table 3.

Figure 13 compares the final PM results for the three different M31 fields. The weighted average of the results is shown in black. This weighted average is also listed in Table 3. The figure shows results in physical units of km s^{-1}, instead of mas yr^{-1}. To transform the units, we assumed a distance of 770 kpc (see references in van der Marel & Guhathakurta 2008), so that 0.1 mas yr^{-1} = 365 km s^{-1}. Distance errors were not propagated in this conversion. The final weighted average PM differs from zero at the $\sim$ 4.3-σ level. Therefore, we have actually measured a motion, and we have not merely put an upper limit on any motion.

4.2. Consistency Checks

To have faith in the results, it is important to assess the internal consistency of the measurements. There are many checks available for this, since we have performed measurements

[1] μ_W is defined to be positive for an object moving towards the West, and therefore has the opposite sign of the PM in the RA direction.

using different exposures, with different instruments, and for different fields.

For a given field i (**SPHEROID**, **OUTERDISK**, or **TIDALSTREAM**), second-epoch instrument j (ACS/WFC or WFC3/UVIS), and coordinate direction k (West or North), we identify the set of l PM measurements μ_{ijkl} (either four or two measurements, depending on the instrument) with random errors $\Delta\mu_{ijkl}$. There are a total of 36 measurements (see Table 2). We combine the different measurements l to obtain the 12 weighted averages $\overline{\mu}_{ijk}$ with random errors $\Delta\overline{\mu}_{ijk}$.

The quantity

$$\chi_1^2 = \sum_{ijkl} \left(\frac{\mu_{ijkl} - \overline{\mu}_{ijk}}{\Delta\mu_{ijkl}} \right)^2 \tag{2}$$

provides a measure of the extent to which different measurements for the same field and with the same instrument agree to within the random errors. We find that $\chi_1^2 = 26.2$. In absence of systematic errors, one expects χ_1^2 to follow a χ^2 probability distribution with $N_{DF} = 36 - 12 = 24$ degrees of freedom. The expectation value for such a distribution is N_{DF}, and the dispersion is $\sim \sqrt{2N_{DF}}$. Hence, the measurements for the same field with the same instrument are statistically consistent with each other. This is also visually evident from inspection of Figure 12, which shows furthermore that the agreement is least good for the **OUTERDISK** field.

The quantity

$$\chi_2^2 = \sum_{ik} \frac{(\overline{\mu}_{i1k} - \overline{\mu}_{i2k})^2}{\Delta\overline{\mu}_{i1k}^2 + \Delta\overline{\mu}_{i2k}^2} \tag{3}$$

provides a measure of the extent to which measurements for the same field with different instruments agree to within the random errors. We find that $\chi_2^2 = 8.5$. In this case $N_{DF} = 6$, so the measurements for the same field with the different instruments are also statistically consistent with each other.

Finally, the quantity

$$\chi_3^2 = \sum_{ik} \left(\frac{\overline{\mu}_{ik} - \overline{\mu}_k}{\Delta\overline{\mu}_{ik}} \right)^2 \tag{4}$$

provides a measure of the extent to which measurements for different fields agree to within the random errors. Here $\overline{\mu}_{ik}$ with random errors $\Delta\overline{\mu}_{ik}$ are the weighted averages over all exposures for given field (top three lines of Table 3). The $\overline{\mu}_k$ are the weighted averages over all fields (bottom line of Table 3)). We find that $\chi_3^2 = 1.9$. In this case $N_{DF} = 6 - 2 = 4$, so the measurements for different fields are also statistically consistent with each other. This is also visually evident from inspection of Figure 13.

The fact that all measurements are statistically consistent indicates that there is no additional scatter in the data that is unaccounted for by the random errors. This justifies the use of weighted averages in combining the different measurements (which propagates only random errors).

4.3. Evaluating Systematic Errors

The final weighted average PM corresponds to a displacement of 0.0074 ACS/WFC pixel over the ~ 7 year time baseline for the **SPHEROID** field. The per-coordinate error in the displacement is only 0.0024 pixel. The displacement errors are even lower for the other fields, which have shorter time baselines.

These displacements are very small, but they can nonetheless be accurately measured. This can be understood based on first principles. A single source can be centroided to an accuracy of order $\sigma/(S/N)$, where σ is the Gaussian dispersion of the object size, and S/N is the signal-to-noise ratio of the observation. For a compact source with $S/N \gtrsim 100$, this yields uncertainties of 0.01–0.02 pixels, consistent with what we found in Figure 7. Therefore, even a single bright compact source in a single exposure can provide an accuracy comparable to the M31 PM displacement. Averaging over multiple sources in many exposures/fields reduces the random uncertainties to thousandths of a pixel and hence allows a solid measurement of the PM displacement.

The key to our robust measurement is, though, control of *systematic errors*, since those are not guaranteed to decrease by averaging multiple measurements. We have paid careful attention throughout our observation planning and subsequent analysis to identify possible sources of systematic errors and adjusted our methodology to minimize them as following:

- The observations were obtained with the F606W filter, which has the best PSF and distortion models for both ACS/WFC and WFC3/UVIS (see Section 2.2).
- The ACS/WFC images were obtained using the same telescope orientation and pointing in both epochs (see Section 2.2). This allows any static astrometric residuals that depend on the position on the detector (e.g., static geometric distortion solution errors) to cancel out in the differential PM measurement.
- The ACS/WFC data were explicitly corrected for the effects of imperfect CTE, reducing any potential astrometric impact (see Section 3.2).
- We used different geometric distortion solutions for the different epochs of data, thus

minimizing any impact due to potential time-variations in the geometric distortion solutions (see Section 3.3).

- We carefully selected our samples of M31 stars and background galaxies to minimize any bias introduced by interlopers (see Section 3.5).

- We built a unique template for every individual source that was measured, thus avoiding any ad hoc assumptions about the properties of PSF or galaxy shapes (see Section 3.6.1).

- We fitted and accounted for PSF variations between different epochs, thereby minimizing any potential PM biases (see Section 3.6.3).

- We measured the relative PM of each background galaxy with respect to only its neighboring stars (the "local correction"), thus minimizing the impact of spurious spatially varying PM residuals (see Section 3.8).

- The above local measurement was made with respect to only stars of similar brightness, thus minimizing the impact of magnitude-dependent PM residuals, including CTE effects (see Section 3.8).

- We obtained the final PM for each field by averaging over background galaxies at many different locations on the detector. This minimizes the potential impact of local peculiarities in detector properties or the astronomical scene (see Section 4.1). Our approach is significantly advantageous over PM studies that use only a single background quasar in an image.

- We determined the random PM error for each exposure from the actual scatter between results from different background galaxies. The resulting errors include all sources of scatter, and not just those from photon-counting statistics (see Section 4.1).

- We used robust statistical measures with outlier rejection throughout our analysis, thus minimizing the potential influence of individual erroneous measurements (e.g., Section 4.1).

- We showed that PM measurements with different instruments, taken at different times and with different telescope orientations, as well as measurements of different fields, all yield statistically consistent results (see Section 4.2). This rules out a large range of possible residual systematic errors, including most possible astrometric residuals specific to a given instrument or detector.

In summary, there is strong reason to believe that the PM measurements and the quoted uncertainties are robust and free of the potential systematics considered in this section.

4.4. M31 motions: Other Contributions and Constraints

The results presented thus far do not directly measure the PM of the M31 center of mass (COM). Instead, in every field we measure the sum of the internal kinematics of the M31 stars and the COM motion. The rotation curve of M31 has an amplitude of ~ 250 km s^{-1} (Corbelli et al. 2010). The contributions from internal kinematics are therefore not necessarily negligible compared to the uncertainties in our measurements (see Figure 13).

In Paper II we model the internal kinematics explicitly, and we derive an unbiased estimate for the COM PM. As it turns out, this estimate is not very different from the weighted average presented in Table 3. We also show in Paper II that this estimate is statistically consistent with the estimate for the transverse motion of M31 derived with the independent methods of van der Marel & Guhathakurta (2008), based on the kinematics of M31 and Local Group *satellites*. This is a further indication that any remaining systematic uncertainties in our measurements are likely to be small.

The observed PMs presented here are heliocentric motions, i.e., *not* corrected for the reflex solar motion in the Milky Way. This known reflex motion falls in the same quadrant of PM space as our measurements (see van der Marel & Guhathakurta 2008). The actual transverse motion of M31 with respect to the Milky Way is therefore closer to zero than what we show in Figure 13. This provides another useful consistency check on our measurements, since there are theoretical reasons to suspect that the transverse motion of M31 with respect to the Milky Way should be small (e.g., Peebles et al. 2001). In fact, we show in Paper II that the transverse motion implied by our data is consistent with zero, meaning that M31 is likely moving on a nearly direct radial orbit towards the Milky Way.

5. Conclusions

We have presented the first direct absolute PM measurements of three fields in M31, our nearest giant companion galaxy in the Local Group. We used new second-epoch *HST* data obtained with two different instruments, combined with very deep pre-existing first-epoch data, spanning a time baseline of 5–7 years. With state-of-the-art analysis methods, using background galaxies as stationary reference frame, we achieved a final PM accuracy of ~ 12 μas yr^{-1}. This is comparable to the accuracies that have been achieved for other Local

Group galaxies using VLBA observations of water masers (Brunthaler et al. 2005, 2007). Water masers were recently discovered in M31 (Darling 2011), but have yet to be used for a PM determination. We have paid careful attention to control of systematic errors throughout our analysis. A large range of consistency checks indicates that our PM measurements and the quoted uncertainties are robust and free of unknown systematics. The new PM results provide improved insights into the history, future, and mass of the Local Group. These topics are explored in detail in Papers II and III of this series.

The techniques presented here for measuring the PM of stars with respect to background galaxies are not only applicable to M31, but can be applied to a wide range of other problems. For example, our group has ongoing *HST* observing programs to use the same techniques to measure the PM of Leo I (GO-12270, PI: S. T. Sohn), the PM of dwarf galaxies near the Local Group turn-around radius (GO-12273, PI: R. P. van der Marel), and the PM of stars in the Sagittarius Stream (GO-12564, PI: R. P. van der Marel). More generally, any deep wide-field space-based imager with a stable configuration, including future missions such as WFIRST and EUCLID, might be able to use the techniques presented here to measure the PMs of foreground objects from multiple epochs of data.

For M31 itself, it would be possible to improve the results presented here through additional *HST* observations by, e.g., increasing the available number of fields, time baselines, or signal-to-noise ratio per epoch. Meanwhile, water masers hold the potential to soon provide PM measurements for individual sources in M31 (Darling 2011). They will yield constraints on the transverse motion of the M31 center-of-mass that are independent from those presented here and in Paper II. Furthermore, water masers might allow measurement of additional effects, such as the M31 PM rotation, and the increase in M31's apparent size caused by its motion towards us.

Support for this work was provided by NASA through a grant for program GO-11684 from the Space Telescope Science Institute (STScI), which is operated by the Association of Universities for Research in Astronomy (AURA), Inc., under NASA contract NAS5-26555. The authors are grateful to Rachael Beaton, Gurtina Besla, Tom Brown, T. J. Cox, Mark Fardal, and Raja Guhathakurta for contributing to the other papers in this series, and for comments that helped improve the presentation of the present paper.

Facilities: HST (ACS/WFC; WFC3/UVIS).

REFERENCES

Anderson, J., & King, I. R. 2000, PASP, 112, 1360

Anderson, J. 2005, in The 2005 HST Calibration Workshop, ed. A. M. Koekemoer, P.Goudfrooij, & L. Dressel (Baltimore, MD: STScI)

Anderson J., & King, I. R. 2006, ACS/ISR 2006-01, PSFs, Photometry, and Astrometry for the ACS/WFC (Baltimore: STScI) (AK06)

Anderson, J. 2007, ACS/ISR 2007-08, Variation of the Distortion Solution of the WFC (Baltimore: STScI)

Anderson, J., & van der Marel, R. P. 2010, ApJ, 710, 1032

Anderson, J. & Bedin, L. R. 2010, PASP, 122, 1035

Baggett, S., Bushouse, R., Gilliland, R., Khozurina-Platais, V., Noeske, K., & Petro, L. 2011, in WFC3 UVIS CTE Whitepaper, http://www.stsci.edu/hst/wfc3/ins_performance/CTE/cte.pdf

Barnard, E. E. 1917, AJ, 30, 175

Bellini, A., Anderson, J. & Bedin, L. R. 2011, PASP, 123, 622

Bertin, E., & Arnouts, S. 1996, A&AS, 117, 393

Brown, T. M., Smith, E., Ferguson, H. C., Rich, R. M., Guhathakurta, P., Renzini, A., Sweigart, A. V., & Kimble, R.A. 2006, ApJ, 652, 323

Brown, W. R., Anderson, J., Gnedin, O. Y., Bond, H. E., Geller, M. J., Kenyon, S. J., & Livio, M. 2010, ApJ, 719, L23

Brunthaler, A., Reid, M. J., Falcke, H., Greenhill, L. J., & Henkel, C. 2005, Science, 307, 1440

Brunthaler, A., Reid, M. J., Falcke, H., Henkel, C., & Menten K. M. 2007, A&A, 462, 101

Corbelli, E., Lorenzoni, S., Walterbos, R., Braun, R., & Thilker, D. 2010, A&A, 511, A89

Cox, T. J., & Loeb, A. 2008, MNRAS, 386, 461

Darling, J. 2011, ApJ, 732, L2

Efron, B., & Tibshirani, R. 1993, An Introduction to the Bootstrap (Chapman & Hall/CRC)

Ferguson, A. M. N., Irwin, M. J., Ibata, R. A., Lewis, G. F., & Tanvir, N. R. 2002, AJ, 124, 1452

Freedman, W. L., & Madore, B. F. 1990, ApJ, 365, 186

Fruchter, A. S., & Hook, R. N. 2002, PASP, 114, 144

Fruchter, A. S. 2011, PASP, 123, 497

Kalirai, J. S., Anderson, J., Richer, H. B., King, I. R., Brewer, J. P., Carraro, G., Davis, S. D., Fahlman, G. G., Hansen, B. M. S., Hurley, J. R., Lépine, S., Reitzel, D. B., Rich, R. M., Shara, M. M., & Stetson, P. B. 2007, ApJ, 657, L93

Kallivayalil N., van der Marel, R. P., Alcock, C., Axelrod, T., Cook, K. H., Drake, A. J., & Geha, M. 2006a, ApJ, 638, 772

Kallivayalil, N., van der Marel, R. P., & Alcock, C. 2006b, ApJ, 652, 1213

Lasker B. M. et al. 2008, AJ, 136, 735

Mahmud N., & Anderson, J. 2008, PASP, 120, 907

Milone, A. P., Villanova, S., Bedin, L. R., Piotto, G., Carraro, G., Anderson, J., King, I. R., & Zaggia, S. 2006, A&A, 456, 517

Peebles, P. J. E., Phelps, S. D., Shaya, E. J., & Tully, R. B. 2001, ApJ, 554, 104

Piatek, S., Pryor, C., Olszewski, E. W., Harris, H. C., Mateo, M., Minniti, D., Monet, D. G., Morrison, H., & Tinney, C. G. 2002, AJ, 124, 3198

Piatek, S., Pryor, C., Olszewski, E. W., Harris, H. C., Mateo, M., Minniti, D., & Tinney, C. G. 2003, AJ, 126, 2346

Piatek, S., Pryor, C., Bristow, P., Olszewski, E. W., Harris, H. C., Mateo, M., Minniti, D., & Tinney, C. G. 2005, AJ, 130, 95

Piatek, S., Pryor, C., Bristow, P., Olszewski, E. W., Harris, H. C., Mateo, M., Minniti, D., & Tinney, C. G. 2006, AJ, 131, 1445

Piatek, S., Pryor, C., Bristow, P., Olszewski, E. W., Harris, H. C., Mateo, M., Minniti, D., & Tinney, C. G. 2007, AJ, 133, 818

Piatek, S., Pryor, C., & Olszewski, E. W. 2008, AJ, 135, 1024

Press, W. H., Teukolsky, S. A., Vetterling, W. T., & Flannery, B. P. 1992, Numerical Recipes in FORTRAN (Cambridge: Cambridge Univ. Press)

Sohn, S. T., Anderson, J., & van der Marel, R. P. 2010, in 2010 Space Telescope Science Institute Calibration Workshop - Hubble after SM4. Preparing JWST, ed. S. Deustua, & C. Oliveira (Baltimore, MD: STScI)

van der Marel, R. P., Anderson, J., Cox, C., Khozurina-Platais, V., Lallo, M., & Nelan, E. 2007, ACS/ISR 2007-07, Calibration of ACS/WFC Absolute Scale and Rotation for Use in Creation of a JWST Astrometric Reference Field (Baltimore: STScI)

van der Marel, R. P., & Guhathakurta, P. 2008, ApJ, 678, 187

van der Marel, R. P., Fardal, M., Besla, G., Beaton, R. L., Sohn, S. T., Anderson, J., Brown, T., & Guhathakurta, P. 2012, ApJ, submitted

Vieira, K., Girard, T. M., van Altena, W. F., Zacharias, N., Casetti-Dinescu, D. I., Korchagin, V. I., Platais, I., Monet, D. G., López, C. E., Herrera, D., & Castillo, D. J. 2010, AJ, 140, 1934

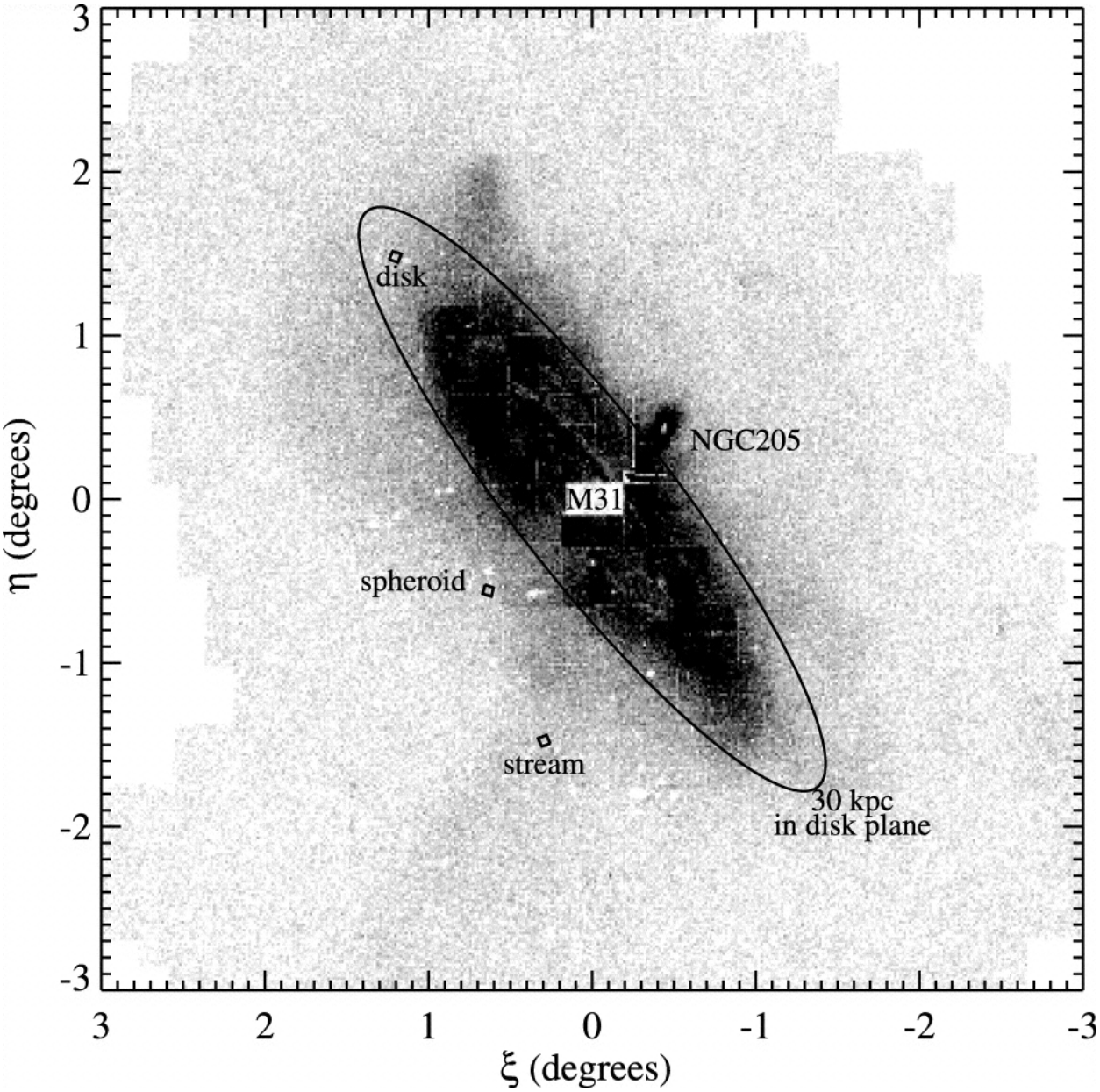

Fig. 1.— Figure taken from Brown et al. (2006). Appropriately scaled and rotated boxes denote our three target fields (labeled). The underlying gray shading represents the density of stars from the map of Ferguson et al. (2002). The ellipse marks the area within 30 kpc of the galactic center in the inclined disk plane (labeled).

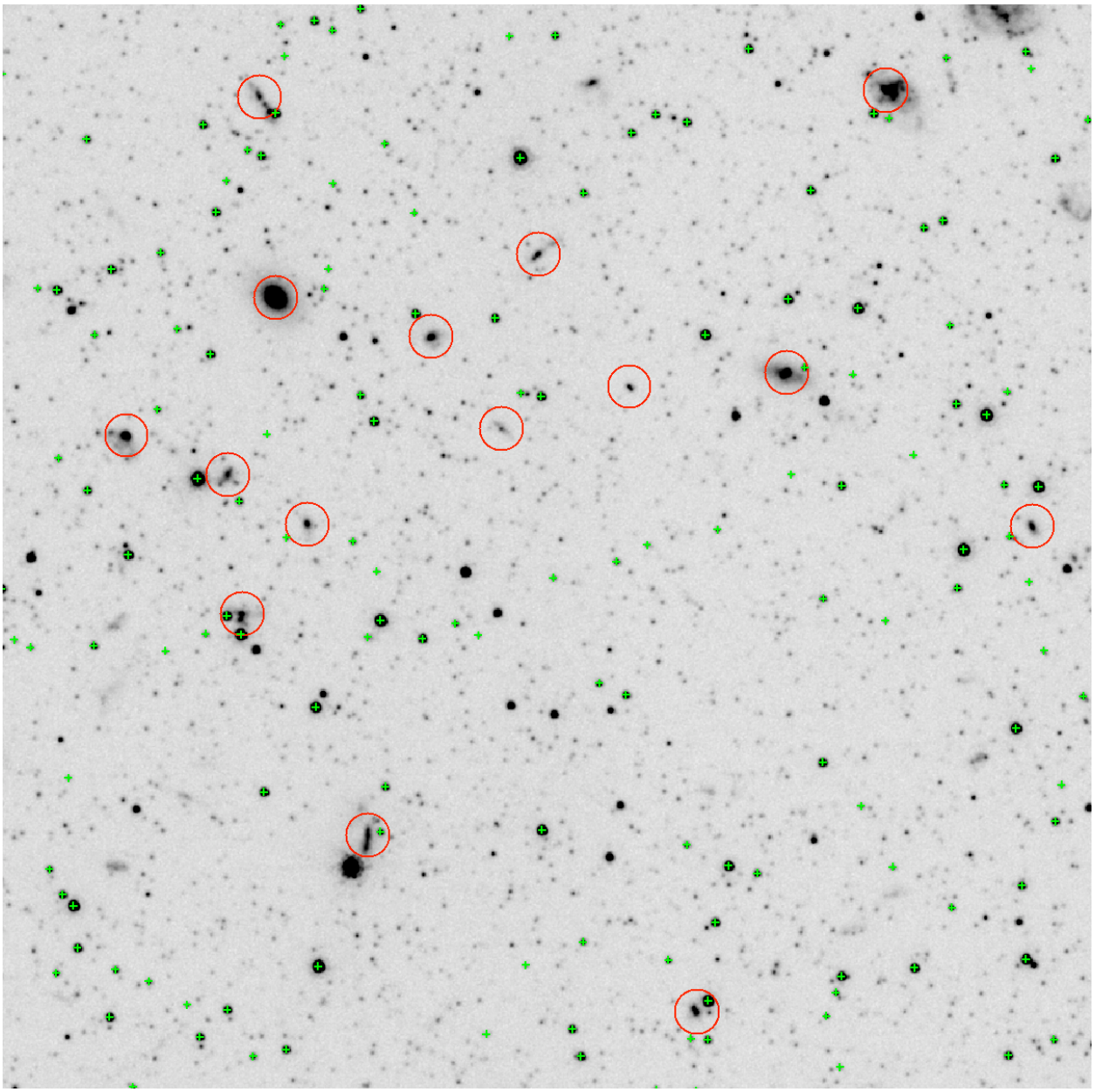

Fig. 2.— A 25″×25″ portion (1.5% of the total image area) of the stacked image for the **SPHEROID** field. Background galaxies used as positional references are enclosed by red circles, while M31 stars that pass the selection criteria of Section 3.5.1 are marked with green plus signs.

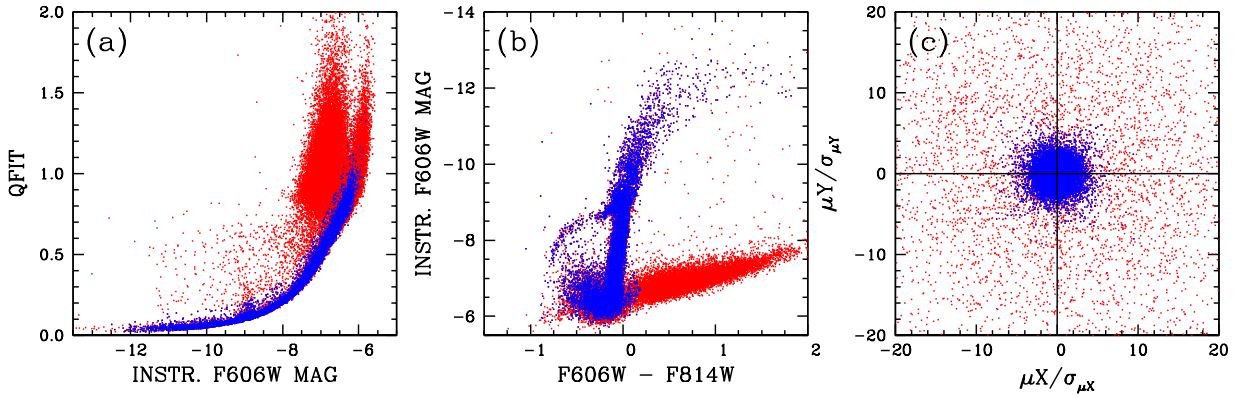

Fig. 3.— Selection of M31 stars in the **SPHEROID** field based on (a) the quality-of-fit (`QFIT`) parameter, (b) the color-magnitude diagram, and (c) relative proper motion (divided by the proper motion error for better scaling) with respect to the average proper motion. In all three panels, blue points are stars that pass all three cuts, while red points are objects that fail to pass at least one cut. Most objects in red located at the bright end of the color-magnitude diagram were rejected because of their relative proper motions. These are likely foreground stars.

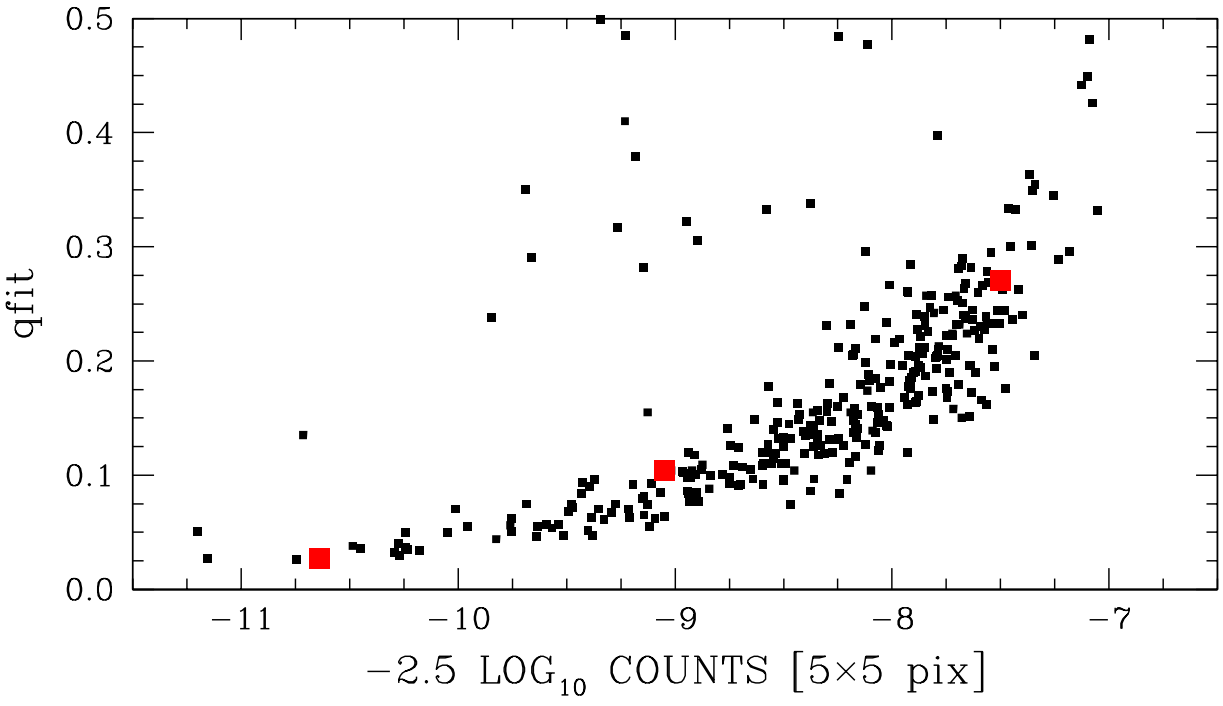

Fig. 4.— Best fit $qfit$ (as defined in Section 3.6.1) versus instrumental magnitude for the background galaxies in one of the first-epoch images (`j8f801caq`). The quantity $qfit$ is a measure of the typical flux residual of the template-fit normalized by the total flux. It therefore behaves as $(S/N)^{-1}$, so that brighter objects yield smaller values of $qfit$. The red squares mark the objects shown in Figure 5.

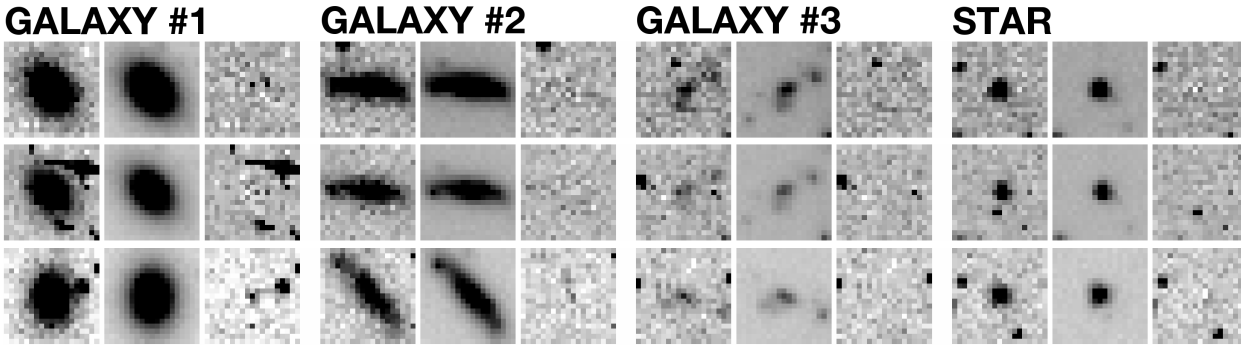

Fig. 5.— Each row shows example results of the template-fitting method. Top row: a first-epoch ACS/WFC exposure; middle row: a second-epoch ACS/WFC exposure; bottom row: a second-epoch WFC3/UVIS exposure. Each row shows results for four different objects. The first three objects (denoted GALAXY #1, #2, and #3), viewed from left to right, are galaxies of decreasing brightness. The rightmost object (denoted STAR) is a star with similar brightness to the second galaxy. Note that the bottom row images are rotated 45° clockwise with respect to those in the top and middle rows because of the difference in orientations between ACS and WFC3 observations (see Section 2.2). For each object in each image we show three images: the observed pixels; the best-fit template; and the residual of the two. The images show a 19×19 pixels patch for illustration, even though the template-fitting was done using only the inner 5×5 pixels. The three galaxies in the top row are the same ones for which the $qfit$ value is indicated with a red square in Figure 4.

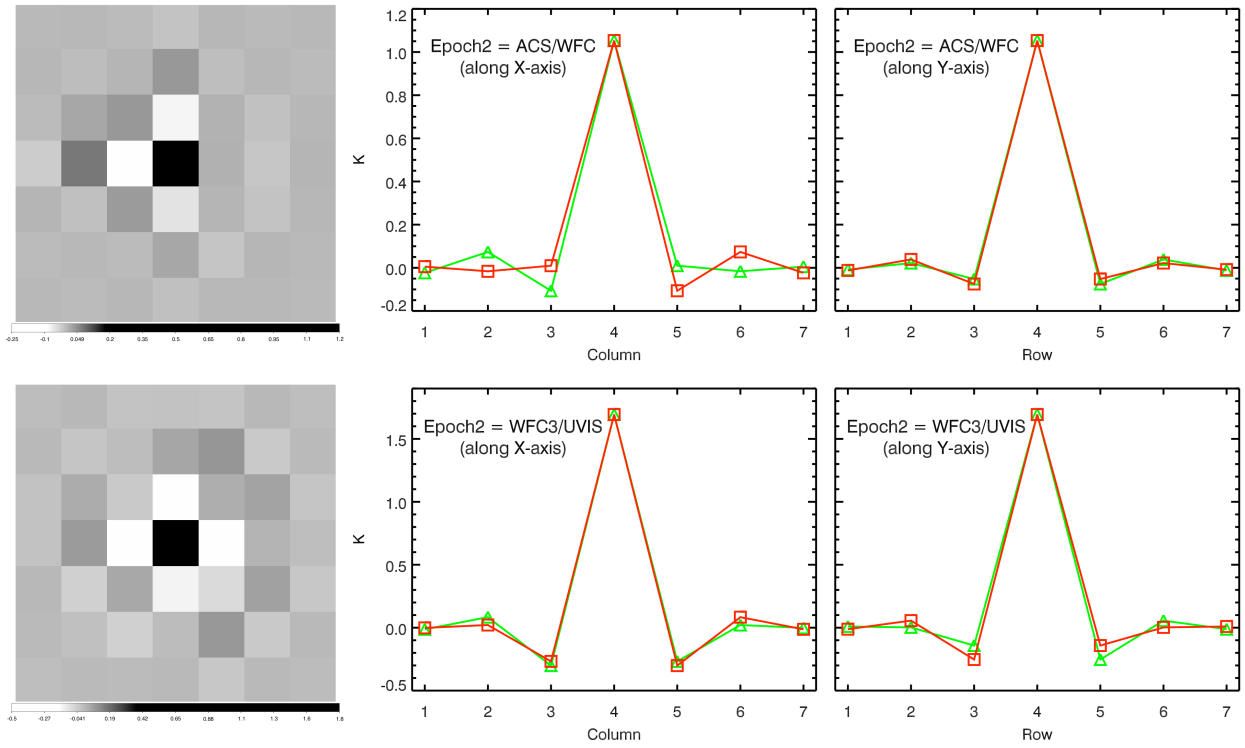

Fig. 6.— Grayscale images (left panels) and one-dimensional cuts (mid and right panels) of the convolution kernels derived for the second-epoch ACS/WFC (top panels) and WFC3/UVIS (bottom panels) data of the **SPHEROID** field. The one-dimensional cuts show in green the central row (mid panels) and the central column (right panels) of the kernel. Red squares show the same values in reverse order (equivalent to flipping the plots about the center along the abscissa). Comparing the plots in different symbols (and colors) provides a measure of asymmetries in the kernels, which could affect astrometry if left uncorrected.

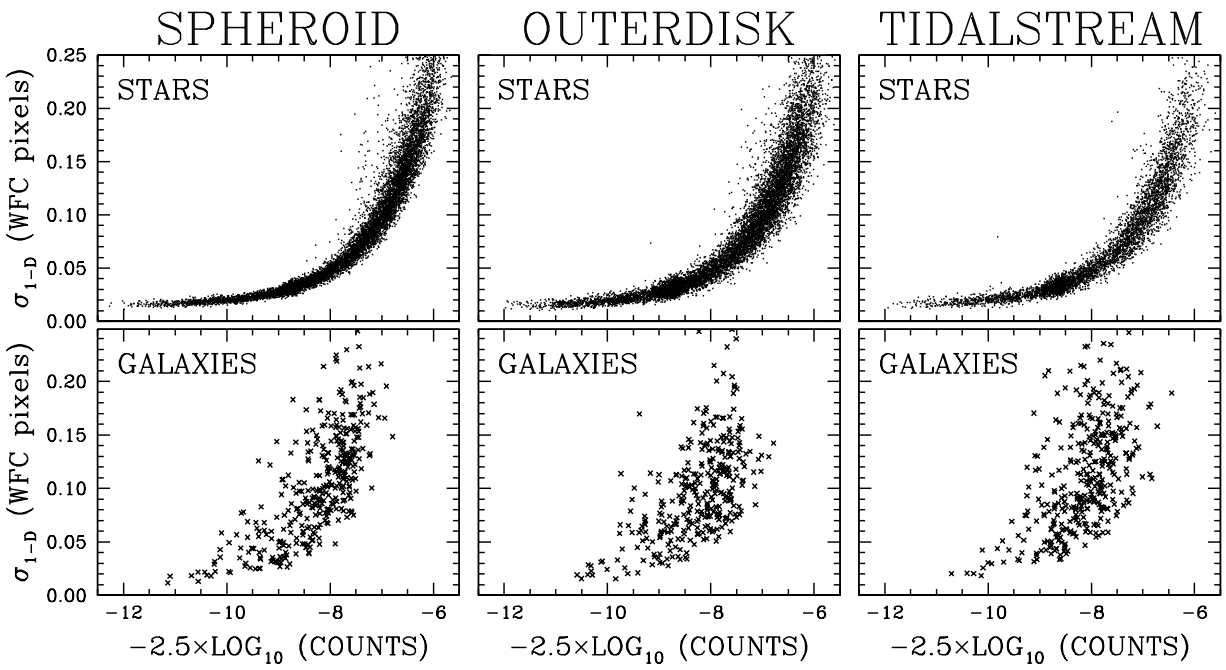

Fig. 7.— The total one-dimensional positional error per exposure as a function of instrumental magnitude, for M31 stars (*upper panels*) and background galaxies (*lower panels*). The error is defined as $\sigma_{1-D} = \sqrt{\frac{1}{2}({\sigma_X}^2 + {\sigma_Y}^2)}$. Here σ_X and σ_Y are the per-coordinate RMS residuals with respect to the average, for the multiple first-epoch measurements.

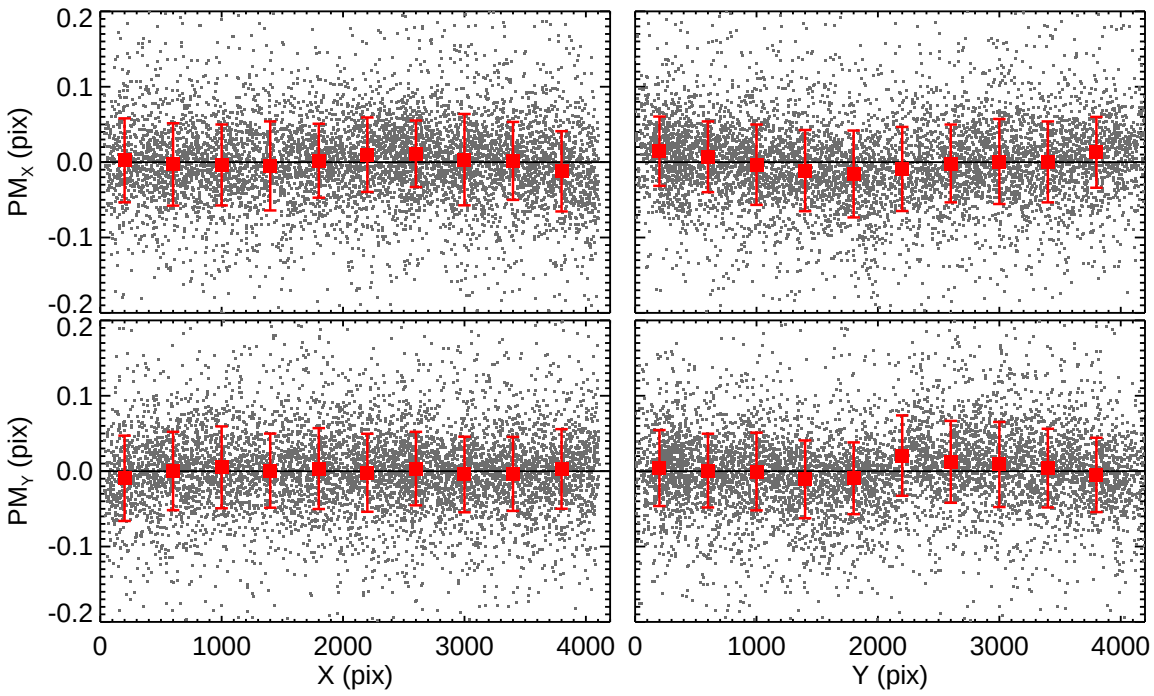

Fig. 8.— Displacements of individual stars (dark gray dots) versus detector location between one of the second-epoch ACS/WFC images (`jb4404vsq`) of the **SPHEROID** field and the average of the first-epoch images, plotted separately for X and Y positions. The units are in native ACS/WFC pixels, and X and Y positions are in the reference frame. We also plot the average displacements of stars and the RMS of the distribution for each 400-pixel bin in red. The RMS is equivalent to the average uncertainty for an individual star. The 1-σ error bars on the red data points equal RMS/$\sqrt{N}$, where N is the number of stars in the bin, and these are smaller than the sizes of the points themselves. So while the displacements average to zero by construction, there are statistically significant low-level trends indicative of residual detector effects. We correct the measurements for these trends using the local corrections described in Section 3.8.

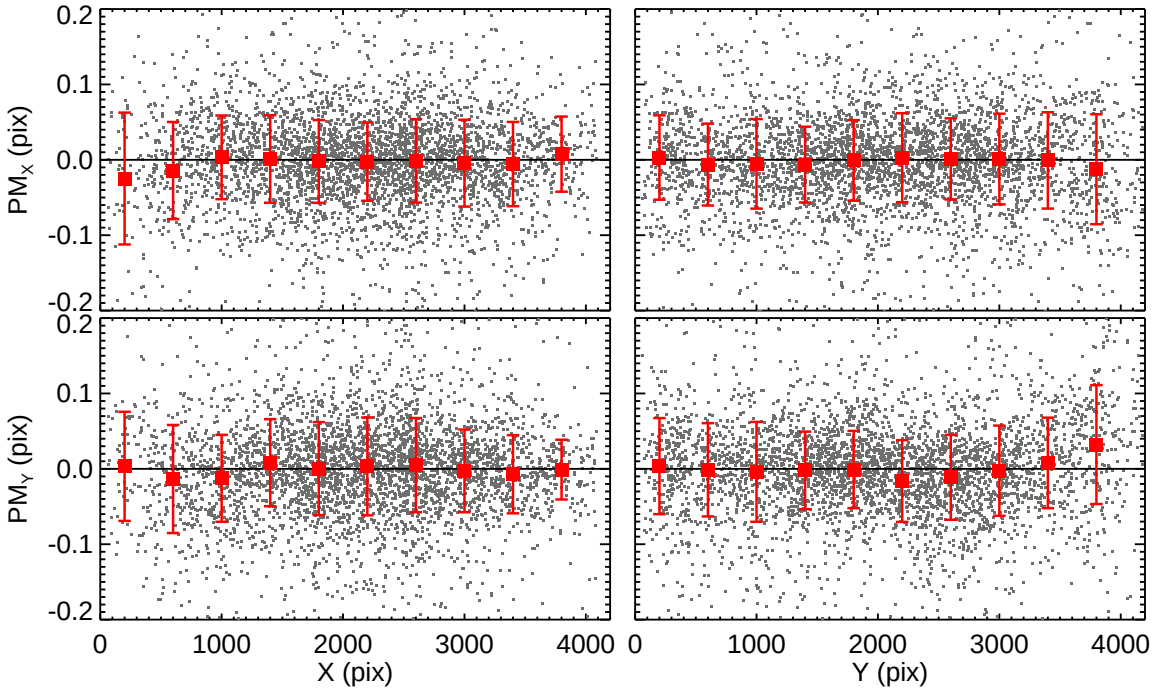

Fig. 9.— As Figure 8, but now for one of the second-epoch WFC3/UVIS images (`ib4401rsq`) of the **SPHEROID** field.

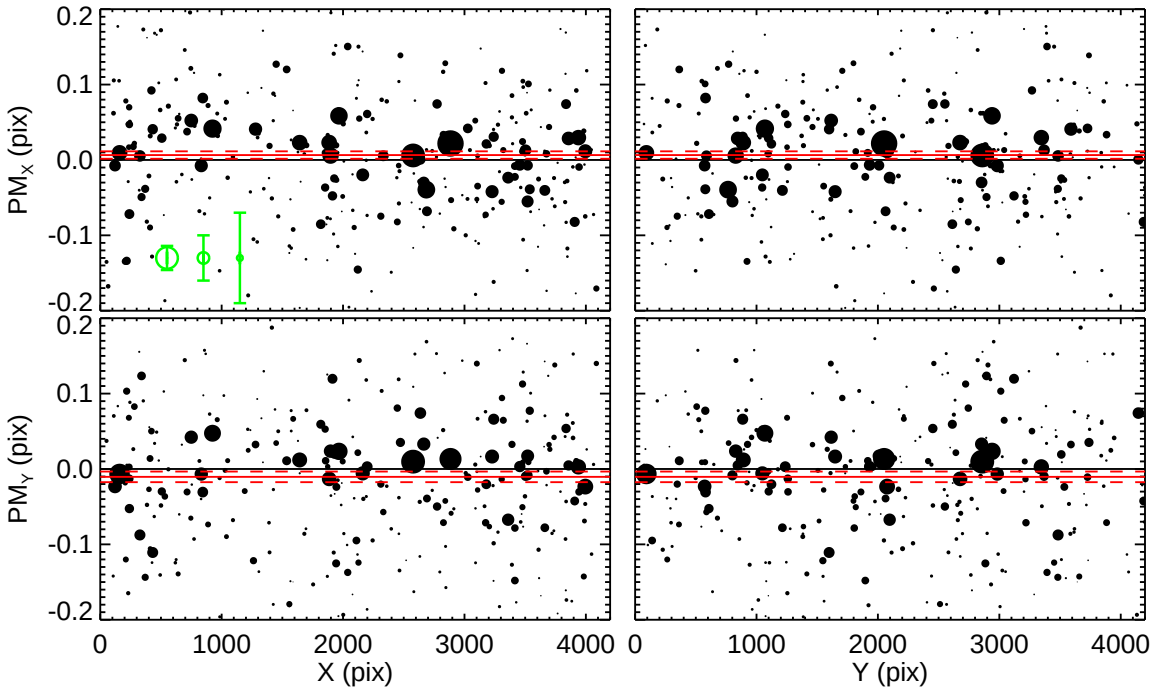

Fig. 10.— Displacements of background galaxies versus detector location between one of the second epoch ACS/WFC images (`jb4404vsq`) of the **SPHEROID** field and the average of the first-epoch images, plotted separately for X and Y positions. The black points show the relative displacements measured for different background galaxies. The weighted average for all galaxies is shown as the red line; dashed red lines indicate the 1-σ error region around the average. This region is smaller than the scatter between the points by a factor of $\sim\sqrt{N}$, where N is the number of background galaxies. The radius of each black point is proportional to $1/\Delta$, where Δ is the PM measurement uncertainty for the particular background galaxy. Hence, the area of each point is proportional to the weight a point receives in the final weighted average. Symbols in green in the top left panel illustrate how the point size relates to the PM uncertainty Δ. The units are in native ACS/WFC pixels, and X and Y positions are in the reference frame.

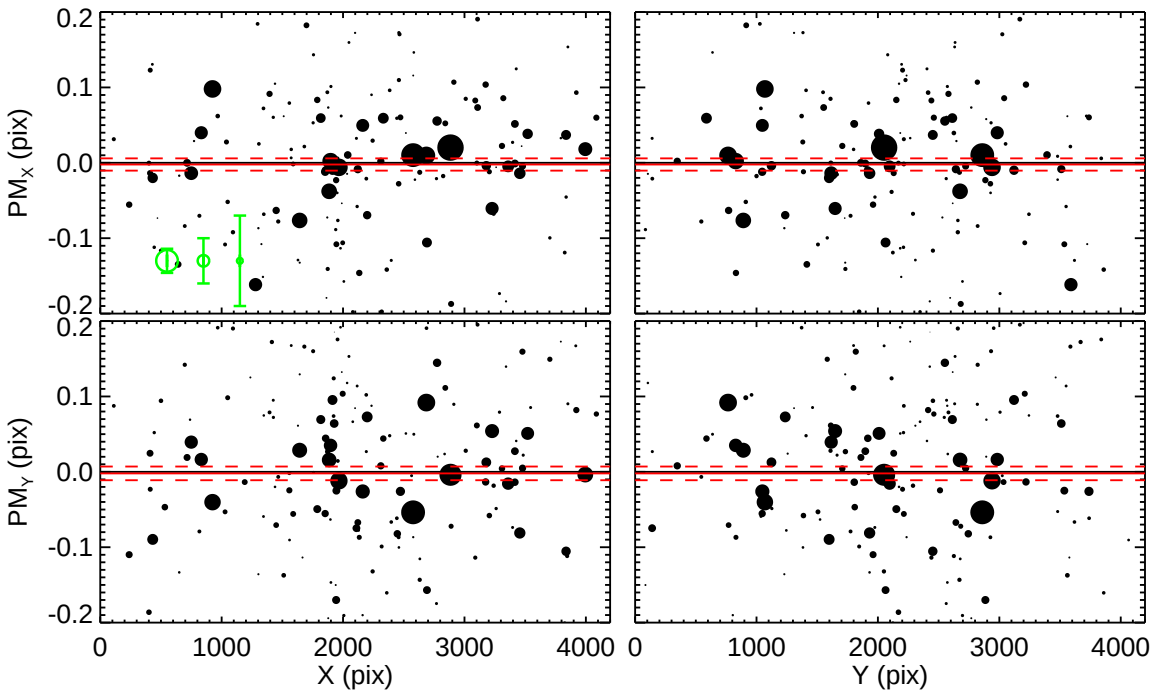

Fig. 11.— As Figure 10, but now for one of the second-epoch WFC3/UVIS images (`ib4401rsq`) of the **SPHEROID** field.

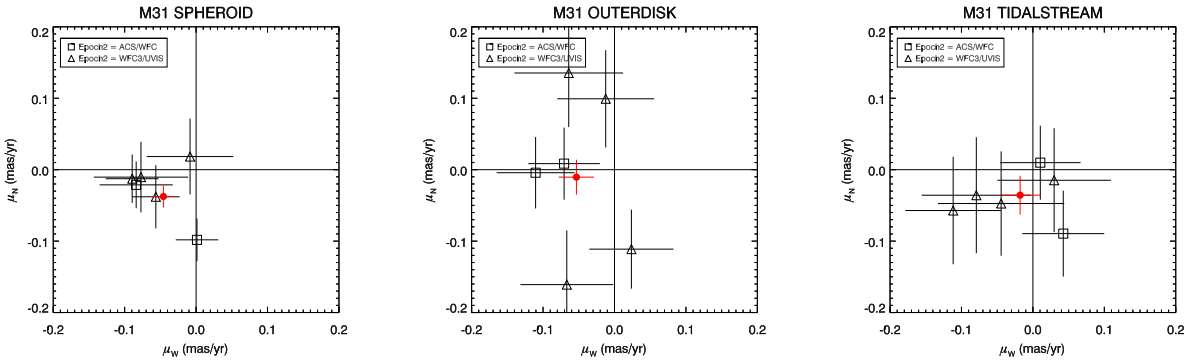

Fig. 12.— Proper-motion results for the three target fields. Each black symbol with an error bar indicates the weighted average PM of M31 stars in the given field, inferred from a single second-epoch exposure as in Figures 10 and 11. Measurements using ACS/WFC (open squares) and WFC3/UVIS (open triangles) are indicated with different symbols. The solid red data point is the weighted average of the six separate measurements for each field.

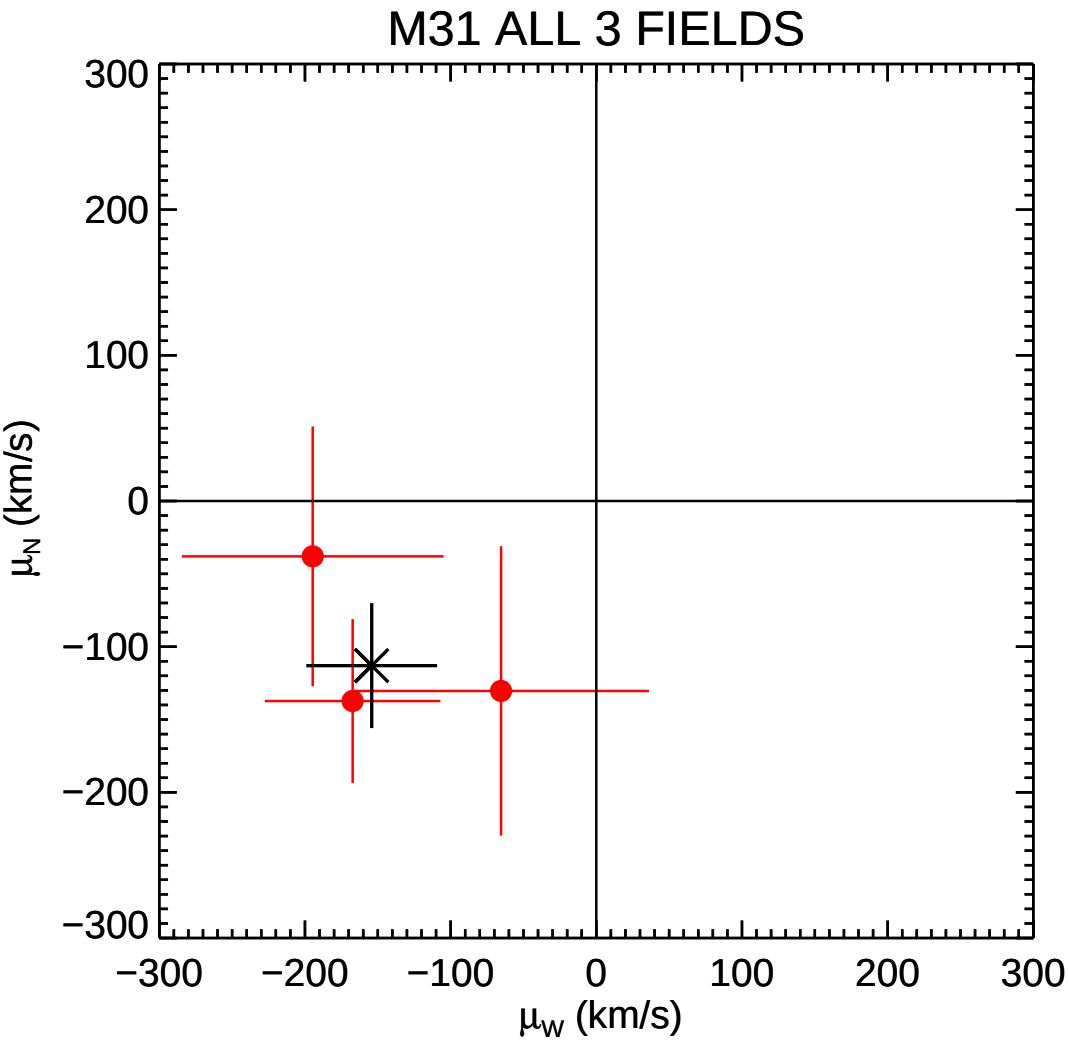

Fig. 13.— Average proper motions, converted to km s^{-1} using a distance to M31 of 770 kpc, for each target field (red closed circles). The error-weighted mean of the 3 fields is shown as the black X mark.

Table 1: Description of Data for the Second Epoch Observations

Target Field	Data set	Detector	PA_V3[a]	Exposure Time (s)	ΔT[b]
SPHEROID	jb4404vsq, jb4404vuq	ACS/WFC	75.07	1289, 1289	7.10
	ib4401rsq, ib4401ruq, ib4401rxq, ib4401s1q	WFC3/UVIS	255.14	1379, 1379, 1450, 1450	7.57
OUTERDISK	jb4405jgq, jb4405jiq	ACS/WFC	247.17	1289, 1289	5.06
	ib4402urq, ib4402uwq, ib4402vqq, ib4402vuq	WFC3/UVIS	67.08	1420, 1420, 1491, 1491	5.55
TIDALSTREAM	jb4406muq, jb4406mwq	ACS/WFC	21.85	1299, 1299	5.99
	ib4403enq, ib4403epq, ib4403esq, ib4403ewq	WFC3/UVIS	216.92	1379, 1379, 1450, 1450	5.47

[a]The position angle of the *HST* V3 axis at the center of detector's field of view.

[b]Baseline between the first and second-epoch data in years.

Note. — All data in the second epoch were obtained with the F606W filter. Field coordinates and descriptions of the first epoch-data are presented in Brown et al. (2006).

Table 2: Proper Motion Results for Individual Second Epoch Images

Field	Data Set	μ_W (mas yr^{-1})	μ_N (mas yr^{-1})	σ_{μ_W} (mas yr^{-1})	σ_{μ_N} (mas yr^{-1})	$N_{\rm used}$[a]
SPHEROID	jb4404vsq	−0.0839	−0.0212	0.0512	0.0327	308
	jb4404vuq	0.0012	−0.0982	0.0297	0.0299	306
	ib4401rsq	−0.0085	0.0184	0.0606	0.0530	176
	ib4401ruq	−0.0564	−0.0379	0.0332	0.0442	176
	ib4401rxq	−0.0772	−0.0104	0.0660	0.0495	186
	ib4401s1q	−0.0895	−0.0126	0.0369	0.0339	172
OUTERDISK	jb4405jgq	−0.0706	0.0085	0.0501	0.0504	310
	jb4405jiq	−0.1105	−0.0043	0.0547	0.0501	286
	ib4402urq	−0.0123	0.0993	0.0679	0.0681	156
	ib4402uwq	−0.0668	−0.1609	0.0649	0.0759	152
	ib4402vqq	−0.0641	0.1353	0.0761	0.0757	161
	ib4402vuq	0.0237	−0.1112	0.0589	0.0553	152
TIDALSTREAM	jb4406muq	0.0425	−0.0895	0.0574	0.0601	321
	jb4406mwq	0.0104	0.0098	0.0564	0.0518	317
	ib4403enq	−0.1116	−0.0572	0.0670	0.0752	185
	ib4403epq	−0.0792	−0.0358	0.0766	0.0812	196
	ib4403esq	−0.0445	−0.0474	0.0883	0.0731	175
	ib4403ewq	0.0298	−0.0148	0.0794	0.0728	185

[a]Number of background galaxies used for deriving the average proper motion.

Table 3: Final Proper Motion Results for the Three Target Fields

Field	μ_W (mas yr^{-1})	μ_N (mas yr^{-1})	σ_{μ_W} (mas yr^{-1})	σ_{μ_N} (mas yr^{-1})
SPHEROID	−0.0458	−0.0376	0.0165	0.0154
OUTERDISK	−0.0533	−0.0104	0.0246	0.0244
TIDALSTREAM	−0.0179	−0.0357	0.0278	0.0272
weighted av.[a]	−0.0422	−0.0309	0.0123	0.0117

[a]Weighted average of the results for the three-target fields. This is *not* an unbiased estimate of the PM of the M31 center-of-mass. It contains contributions also from the internal motions of stars in M31, which are modeled and corrected in Paper II.